Sensors and Materials, Vol. 25, No. 6 (2013) 403–410
MYU Tokyo

S & M 0933

Fiber Cross-Section Shape Effect on Rate-Dependent Behavior of Polymer Matrix Composites with Fiber Bragg Grating Sensors

Zhi Zhai, Zhengjia He*, Xuefeng Chen, Junjie Ye[1] and Xiaojun Zhu

State Key Laboratory for Manufacturing Systems Engineering, Xi´an Jiaotong University,
Xi´an 710049, P.R.China
[1]School of Electro-Mechanical Engineering, Xidian University,
Xi´an 710071, P.R.China

(Received November 5, 2012; accepted February 4, 2013)

Key words: polymer matrix composites, rate dependence, FBGs, off-axis loading, fiber shape

A strain measurement system with fiber Bragg grating (FBG) sensors is developed to monitor the quasistatic/dynamic strain in a glass/epoxy for the experimental analysis of the rate-dependent behavior of polymer matrix composites (PMCs). The rate-dependent inelastic constitutive relationship of epoxy is built using an internal state variable viscoplasticity model with experimental responses. The micromechanical investigation of fiber shape effect on the rate-dependent behavior of glass/epoxy for various off-axis angles is performed at 10^{-5} and 1/s. The results indicate that a higher strain rate causes a greater flow stress in PMCs. The fiber shape evidently affects the inelastic deformation at large off-axis angle with the biggest stiffness provided by the square fiber, but has little impact on the elastic deformation for all off-axis angles. The effect of fiber shapes on overall responses is enhanced with increasing off-axis angles but weakens with increasing strain rate.

1. Introduction

Fiber-reinforced polymer composites (PMCs) are considered high-performance materials(1) and have drawn increasing attention in the fields of structure health monitoring and mechanical behavior and structural analysis.(2,3) Large-scale PMC structures, such as wind turbine blades and airplane bodies, are often subjected to dynamic loads in service, and the behavior of PMCs shows rate sensitivity as the loading rate changes.(4,5) An exact analysis of the rate-dependent performance of PMCs relies on strain measurement accuracy.

Owing to their sensitivity to electromagnetic interference and low-speed response, traditional strain gauges have low reliability in strain measurement at high-rate loading and hardly capture the exact dynamic strain. On the other hand, fiber Bragg grating (FBG)

*Corresponding author: e-mail: hzj@mail.xjtu.edu.cn

sensors have been developed as promising measuring devices for the *in situ* real-time monitoring of various physical quantities, particularly strain, in composite structures in recent decades. Owing to their small size and light weight, quick and accurate measurement, and resistance to corrosion, FBGs can be both directly surface mounted or embedded into structures and constitute a distributed sensor network for large-area measurement. Besides, FBGs have high sensitivity to track strain variation in real time that closely reflects the structure deformation.[6,7] Therefore, FBGs are employed to measure the strain of PMC samples at different strain rates.

Although macromechanics have been developed as a sophisticated technique for the application of mechanical properties,[8,9] dynamic feature,[10] structure optimization[11] and damage simulation[12] in homogeneous materials and the dynamic response of composites,[13,14] it is difficult to describe the periodic or quasi-periodic microstructures of PMCs, which have a strong impact on the overall behavior of composites. The micromechanical approach utilizes representative volume elements (RVEs) representing the minimal repeating unit of composites to link the macroquantities of composites and the microstructure of materials. Consequently, micromechanics have been widely used for the evaluation of mechanical properties and the simulation of nonlinear responses of PMC with local microstructure effects.[15–17] In this study, the modified Bodner-Parton model was adopted to characterize the rate-dependent response of PMCs,[18] and to study the effects of fiber shapes and off-axis angle on these responses of PMCs at various strain rates. The micromechanical analysis on the rate-dependent response of PMCs also prepares for the damage monitoring of wind turbine blades with an FBG strain sensor network in the future.

2. Materials and Methods

2.1 *Materials and specimens*

The specimens of pure epoxy and its 10-ply unidirectional glass/epoxy composite laminate were selected to test the rate-dependent properties of polymer and PMCs. According to the standards of ASTM D3039 and ASTM D5379, the tensile specimens for epoxy and PMCs both have straight sides with dimensions of 250×25×3 mm^3, and the epoxy specimens under shear loading are V-notched beams with dimensions of 76×20×2 mm^3. The aluminum alloy tabs of 1 mm thickness were attached to the ends of the specimen. The 30 and 60° off-axis PMC coupons with 0.4 fiber volume fraction were selected in the experiment. The elastic constants of component glass fiber and epoxy are E_f = 71.42 GPa, ν_f = 0.2, E_m = 3.4 GPa, and ν_m = 0.22.

2.2 *Experiment apparatus*

The experiment apparatus for testing static-dynamic mechanical properties of PMCs was fundamentally composed of two parts: materials testing system (MTS) and strain measurement system including FBG strain sensors, material specimens, the SM130 optical sensing interrogator and the signal acquisition and processing module. Figures 1(a) and 1(b) respectively show the overall structure and specimens attached with FBG sensors. The centric wavelength of FBG strain sensors is 1550±0.5 nm. The strain of samples can be measured by the centric wavelength of FBG sensors which varies with

(a) (b)

Fig. 1. Experimental setup for testing mechanical properties of PMCs: (a) overall structure and (b) specimens attached wiht FBGs.

the strain variation accordingly. The connection between the Bragg wavelength shift $\Delta\lambda_B$ and axial strain of FBG ε is a function of the effective conversion coefficient p_e between them, which is expressed as

$$\varepsilon = \frac{\Delta\lambda_B}{p_e} \times 1000, \tag{1}$$

where p_e is 1.2 pm/$\mu\varepsilon$ in the experiment. The strain range of the sensor is ±3000 $\mu\varepsilon$. The full width at half maximum bandwidth (FWHM BW) of the FBGs is < 0.3 nm and its reflectivity is > 80%. Thus, the narrow bandwidth and high relectivity of the sensors achieve a high accuracy. The SM130 optical sensing interrogator acquired the quasistatic/dynamic variation of centric wavelength of FBGs. The major technical specifications of SM130 are listed in Table 1, where the long-term stability and repeatability of SM130 meet the demand for the high accuary of strain measurement.

3. Micromechanical Analysis Model

The off-axis response of PMCs is predicted using the GMC model,[19] the procedure of which contains the following main steps. First, the unit cell (i.e., RVE) is divided into $N_\beta \times N_\gamma$ subcells to account for the periodic microgeometry of PMCs. Then, the closed form of the constitutive equations is derived under the displacement and stress continuity conditions of subcells. Finally, by solving the equations, we obtain the relationships of the overall (macroscopic) and local (microscopic) stress and strain quantities.

The overall effective stress and strain are derived in terms of the local stress and strain of subcells by constitutive equations of the overall and local quantities:

Table 1
Technical specifications of SM130 interrogator.

Technical index	Value
Wavelength range	1510–1590 nm
Wavelength stability	2 pm typical, 5 pm max
Wavelength repeatability	1 pm (0.05 pm with 1000 averages)
Scan frequency	1 kHz
Max sensors per channel	80 (4 channels)
Operating temperature	0–50 °C
Operating humidity	0–80%, no condensing

$$\begin{aligned}\overline{\sigma} &= \frac{1}{hl}\sum_{\beta=1}^{N_\beta}\sum_{\gamma=1}^{N_\gamma} h_\beta l_\gamma \overline{\sigma}^{(\beta\gamma)} = \frac{1}{hl}\sum_{\beta=1}^{N_\beta}\sum_{\gamma=1}^{N_\gamma} h_\beta l_\gamma C_{ijkl}^{(\beta\gamma)} \overline{\varepsilon}_{kl}^{(\beta\gamma)} \\ &= \frac{1}{hl}\sum_{\beta=1}^{N_\beta}\sum_{\gamma=1}^{N_\gamma} h_\beta l_\gamma C_{ijkl}^{(\beta\gamma)} A^{(\beta\gamma)} \overline{\varepsilon} = C_{ijkl}^{*} \overline{\varepsilon}_{kl}\end{aligned} \tag{2}$$

where $C_{ijkl}^{(\beta\gamma)}$ represents the components of the microscopic stiffness coefficient matrix in the subcell $(\beta\gamma)$, $A^{(\beta\gamma)}$ is the connecting matrix, and C_{ijkl}^{*} denotes the components of the macroscopic effective stiffness coefficient matrix, which is described using the subcell stiffness matrix $C^{(\beta\gamma)}$ as follows:

$$C^{*} = \frac{1}{hl}\sum_{\beta=1}^{N_\beta}\sum_{\gamma=1}^{N_\gamma} h_\beta l_\gamma C^{(\beta\gamma)} A^{(\beta\gamma)}. \tag{3}$$

4. Internal State Variable Viscoplastic Model

The modified Bodner-Partom viscoplastic model[18] introduces internal state variables (ISVs) characterizing the material microstructure change to represent the micromechanical effect. It utilizes two state variables involving internal stress and hydrostatic stress to express the evolution of viscoplastic strain. The flow law for viscoplastic strain rate components is formulated as follows:

$$\dot{\varepsilon}_{ij}^{I} = 2D_0 \exp\left[-\frac{1}{2}\left(\frac{Z}{\sigma_e}\right)^{2n}\right]\left(\frac{S_{ij}}{2\sqrt{J_2}} + \alpha\delta_{ij}\right), \tag{4}$$

where $\dot{\varepsilon}_{ij}^{I}$ and S_{ij}, respectively, denote the components of inelastic strain rate tensor and deviatoric stress, δ_{ij} is the Kronecker delta, and σ_e is defined as the effective stress. D_0 and n are both material constants. The state variables Z and α are the functions of the effective value of the deviatoric inelastic strain rate $\dot{\varepsilon}_{ij}^{I}$, where the coefficient q is a

material constant describing the hardening rate of materials, and Z_0, Z_1, α_0, and α_1 are the initial and maximum values of Z and α, respectively. The material constants in eq. (4), D_0, n, Z_1, α_1, Z_0, α_0, and q, need to be determined.

5. Results

5.1 *Validation*

Suppose that the fiber is linear elastic, and the epoxy matrix is viscoplastic. According to the determination procedure in ref. 18, the material constants of the ISV viscoplastic model are attained by finding the curves to best fit the experiment data of pure epoxy for tensile and shear loading. Figure 2(a) shows the tensile and shear responses of epoxy at strain rates of 0.00001 and 1/s, and the material constants of the viscoplastic model are listed in Table 2. Then, the tensile responses of glass/epoxy at 30 and 60° off-axis simulated by the combination of the GMC model and the viscoplastic model with the material contants determined above are compared with the experiment data as shown in Fig. 2(b). The elastic stages of epoxy and glass/epoxy at two strain rates appear to be similar, but their viscoplastic deformations are significantly rate-dependent. Figure 2 also shows that the proposed method is capable of simulating the nonlinear behavior of PMCs. Thus, the GMC method is available and effective for the analysis of the rate-dependent mechanical properties of PMCs.

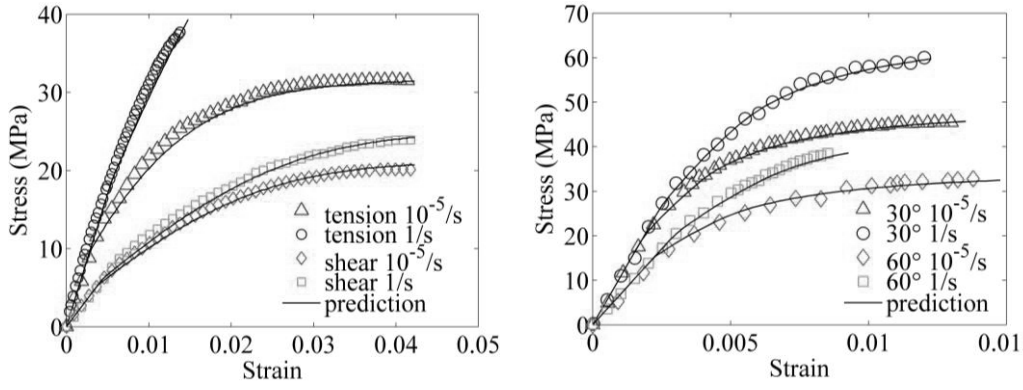

Fig. 2. Rate-dependent stress-strain curves of coupon specimens: (a) epoxy and (b) glass/epoxy.

Table 2
Viscoplastic parameters of constitutive equations of epoxy.

Material	D_0 (s^{-1})	Z_0 (GPa)	Z_1 (GPa)	α_0	α_1	n	q
Glass fiber	0.0	1×10^9	1×10^9	1×10^9	1×10^9	1×10^9	1
epoxy	1×10^6	0.391	0.803	0.04	0.11	0.68	280

5.2 *Fiber cross-section shape effect*

The effect of fiber cross-section shape on the rate-sensitive behavior of PMCs with respect to four fiber shapes, namely, square, cross, circle, and ellipse, the unit cells of which include 4×4, 5×5, 14×14, and 14×14 subcells, respectively (shown in Fig. 3), are determined for 30, 45, 60, and 90° off-axial loading at 10^{-5} and 1/s strain rates. The properties of the fiber and epoxy are given in Table 2. Figures 4(a)–4(d) show the comparisons of low- and high-rate stress-strain curves with different shapes for 30, 45, 60 and 90° off-axis angles. The stress of all the curves first increases rapidly and then slowly approaches a constant called maximum stress. It is observed that the responses at 30, 45, and 60° with different fiber cross-section shapes have a slight difference in the elastic region, and are similar to each other in the plastic region at each strain rate. It implies that the fiber shape effect and its variation with strain rate are very small and the differences in the responses are too little to be distinguished. However, at 90°, the effects of various shapes on the responses are clearly distinct under both high and low rates. The stiffest response for the square fiber is much higher than those for other shapes, and the most flexible responses for the circle and ellipse are similar. The results indicate that the fiber shape effect on nonlinear behavior becomes evident with the increase in off-axis angles at both low and high strain rates. From the maximum stress differences of the four fibers, it denotes that the increasing strain rate reduces the effect of fiber shapes. Figures 5(a) and 5(b) display the longitudinal modulus and plastic strain differences between various strain rates changing with off-axis angle for the four shapes. A higher strain rate produces a lower plastic strain for all the fiber shapes, so the percent difference in plastic strain is defined as $D_R = \frac{\varepsilon_L^P - \varepsilon_H^P}{\varepsilon_H^P} \times 100\%$, where ε_L^P and ε_H^P are the plastic strains of the low and high strain rates at the strain of 0.025, respectively. It is noted that the longitudinal moduli for the four shapes all first sharply drops as the angle becomes < 45° and then decreases slightly when the angle increases. The modulus difference for different shapes is below 20%. It implies that the fiber shape effect on the modulus is small. The elliptical fiber yields the highest modulus and the others have a lower modulus with a similar value at all off-axis angles. On the other hand, it is seen that in the plastic stage (seen in Fig. 5(b)), the differences first sharply drop as the angle becomes < 30° and then increase slightly. The strain rate has a larger impact on the fiber

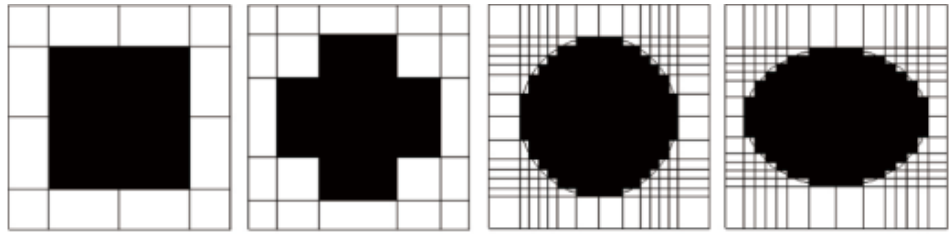

(a) (b) (c) (d)

Fig. 3. Subcell arrangements for fiber shapes: (a) square, (b) cross, (c) circle, and (d) ellipse.

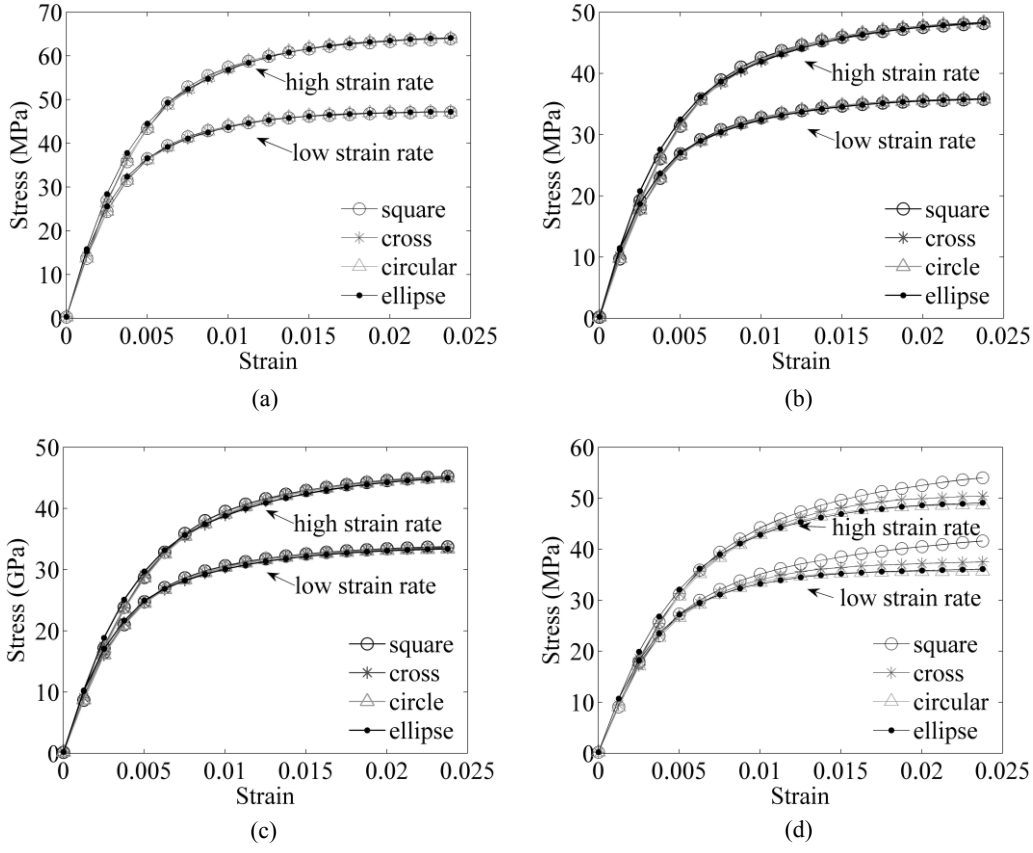

Fig. 4. Tensile stress-strain curves of glass/epoxy at low and high strain rates with different fiber shapes for (a) 30°, (b) 45°, (c) 60°, and (d) 90°.

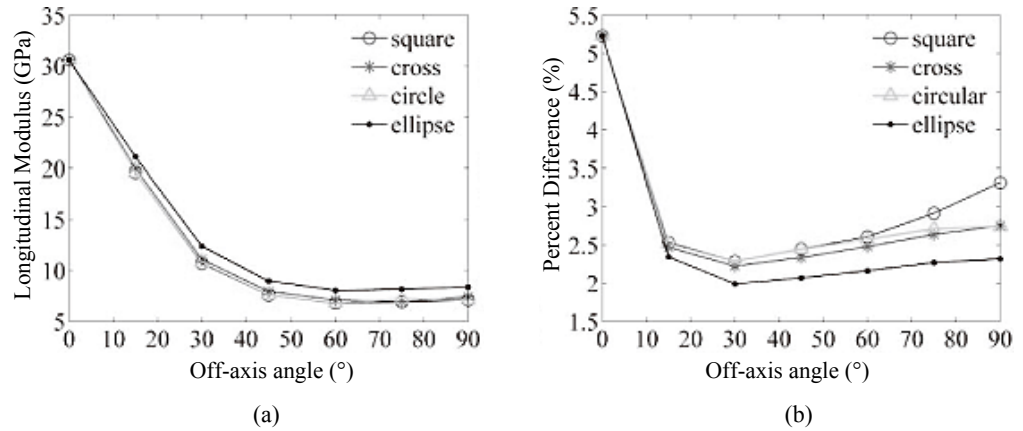

Fig. 5. Changes in elastic and plastic properties with off-axis angles for various fiber shapes: (a) elastic modulus and (b) plastic strain difference.

shape effect under a larger off-axis angle. The square fiber provides the greatest effect, and the elliptical fiber provides the smallest effect.

6. Conclusions

On the basis of FBG strain measurement, the viscoplastic behavior of PMCs is constructed using an internal state variable model. The micromechanical analysis was conducted to investigate the fiber shape effect on the rate-sensitive nonlinear response of a glass/epoxy at various off-axis angles. The results show that the fiber shape, off-axis angle and loading rate evidently affect the viscoplastic deformation of PMCs. The fiber shape effect increases markedly when the off-axis angle increases. A higher strain rate leads to a less effect on the responses with different fiber shapes over the range of off-axis angles. The flow stress is the largest for the square fiber but the least for the circular fiber under the same condition. Moreover, fiber shapes induce a slight variation of elastic properties. The square fiber has the most effect on the viscoplastic behavior and the elliptical fiber has the least one.

Acknowledgements

This work was supported by the National Natural Science Foundation of China (Nos. 51035007 and 51175401), the Research Fund for the Doctoral Program of Higher Education of China (No. 20120201110028) and the Program for Changjiang Scholars and Innovative Research Team in University.

References

1 C. M. Liu, M. S. Chiang and W. C. Chuang: Int. J. Eng. Technol. Innovation. **2** (2012) 48.
2 N. Mrad: T. Can. Soc. Mech. Eng. **31** (2007) 1.
3 F. Mustapha, K. D. Mohd Aris, N. A. Wardi, M. T. H. Sultan and A. Shahrjerdi: J. Vibroeng. **14** (2012) 1342.
4 M. Kawai, J. Q. Zhang, Y. Xiao and H. Hatta: J. Compos. Mater. **44** (2010) 75.
5 D. Asprone, E. Cadoni, A. Prota and G. Manfredi: J. Compos. Constr. **13** (2009) 558.
6 T. K. Gangopadhyay, M. Majumder, A. Kumar Chakraborty, A. K. Dikshit and D. K. Bhattacharya: Sens. Actuators, A **150** (2009) 78.
7 X. Zhao, J. Gou, G. Song and J. P. Ou: Compos. Eng. B **40** (2009) 134.
8 K. Muthukkumaran and M. G. Krishnan: Int. J. Eng. Technol. Innovation. **2** (2012) 31.
9 M. Andrikaitis and A. Fedaravičius: J. Vibroeng. **14** (2012) 1390.
10 X. W. Zhang, X. F. Chen, Z. J. He and H. R. Cao: J. Vibroeng. **14** (2012) 363.
11 C. K. Varghese and K. Shankar: Int. J. Eng. Technol. Innovation. **1** (2011) 65.
12 B. Li, H. Cao and Z. J. He: J. Vibroeng. **13** (2011) 729.
13 M. N. Ensan, D. G. Zimcik, M. Lahoubi and D. Andrieu: Trans. Can. Soc. Mech. Eng. **32** (2008) 283.
14 S. Ghinet and N. Atalla: Trans. Can. Soc. Mech. Eng. **30** (2006) 473.
15 R. Rodríguez-Ramos, P. Yan, J. C. López-Realpozo, R. Guinovart-Díaz, J. Bravo-Castillero, F. J. Sabina and C. P. Jiang: Compos. Struct. **93** (2011) 709.
16 J. Ye, X. Chen, Z. Zhai, B. Li, Y. Duan and Z. He: Mech. Compos. Mater. **46** (2010) 405.
17 J. Orlik: Compos. Struct. **92** (2010) 1581.
18 R. K. Goldberg, G. D. Roberts and A. Gilat: J. Aerosp. Eng. **18** (2005) 18.
19 M. J. Pindera and B. A. Bednarcyk: NASA Research Technical Report No. NASA CR-202350 (1997).